• Original Paper •

Automatic Identification of Clear-Air Echoes Based on Millimeter-wave Cloud Radar Measurements

Ling YANG[*,1,5], Yun WANG[1,5], Zhongke WANG[2], Qian YANG[1,5], Xingang FAN[1,3],
Fa TAO[1,6,7], Xiaoqiong ZHEN[1,4,5], and Zhipeng YANG[1,5]

[1]*Electronic Engineering College*, *Chengdu University of Information Technology*, *Chengdu* 610225, *China*

[2]*Information Security Engineering College*, *Chengdu University of Information Technology*, *Chengdu* 610225, *China*

[3]*Department of Geography and Geology*, *Western Kentucky University*, *Bowling Green*, *KY* 42101, *USA*

[4]*Institute of Atmospheric Physics*, *Chinese Academy of Sciences*, *Beijing* 100029, *China*

[5]*CMA Key Laboratory of Atmospheric Sounding*, *Chengdu University of Information Technology*, *Chengdu* 610225, *China*

[6]*Collaborative Innovation Center on Forecast and Evaluation of Meteorological Disasters*, *Nanjing University of Information Science and Technology*, *Nanjing*, 210044, *China*

[7]*Meteorological Observation Centre*, *CMA*, *Beijing* 100081, *China*

ABSTRACT

Millimeter-wave cloud radar (MMCR) provides the capability of detecting the features of micro particles inside clouds and describing the internal microphysical structure of the clouds. Therefore, MMCR has been widely applied in cloud observations. However, due to the influence of non-meteorological factors such as insects, the cloud observations are often contaminated by non-meteorological echoes in the clear air, known as clear-air echoes. It is of great significance to automatically identify the clear-air echoes in order to extract effective meteorological information from the complex weather background. The characteristics of clear-air echoes are studied here by combining data from four devices: an MMCR, a laser-ceilometer, an L-band radiosonde, and an all-sky camera. In addition, a new algorithm, which includes feature extraction, feature selection, and classification, is proposed to achieve the automatic identification of clear-air echoes. The results show that the recognition algorithm is fairly satisfied in both simple and complex weather conditions. The recognition accuracy can reach up to 95.86% for the simple cases when cloud echoes and clear-air echoes are separate, and 88.38% for the complicated cases when low cloud echoes and clear-air echoes are mixed.

Key words: millimeter-wave cloud radar, clear-air echoes, neural network, laser ceilometer, all-sky camera, feature extraction, feature selection

Article Highlights:

- Measurements from a laser ceilometer, MMCR, L-band radiosonde, and all-sky camera are used to delineate clear-air echoes and cloud echoes.
- Features are filtered using the Relief algorithm to obtain the optimal feature subset, from which the neural network algorithm is trained to realize the automatic recognition of the clear-air echoes.

---

1. Introduction

Since the first Ka-band millimeter-wave cloud radar (MMCR) was developed by Paulsen in the 1970s for meteorological observation (Paulsen et al., 1970), it has been widely used in the field of cloud observation. Owing to its short wavelength and high sensitivity, MMCR has the capability of detecting the internal microphysical structure of clouds, such as particle sizes, liquid water content, and drop spectral distributions (Frisch et al., 1995; Sassen et al., 1999; Kollias and Albrecht, 2000; Kollias et al., 2001; Hogan et al., 2005; Lu et al., 2015). However, the atmospheric boundary layer often has distinct features of daily variation and tur-

bulence. In addition, hydrometeors are not the only source of atmospheric backscattering (Luke et al., 2008). Although cloud radars are insensitive to the Bragg scattering in the lower troposphere, MMCR often detects echoes on sunny days without the presence of clouds or precipitation, and these echoes are termed as clear-air echoes by the American Meteorological Society (Jacoby-Koaly et al., 2002).

All the cloud-radar data used in this study are from the MMCR located in the southern suburb observatory in Beijing, which belongs to the Meteorological Observation Center of the China Meteorological Administration (CMA). The radar system uses a solid-state, phase-coherent, and quasi-continuous wave system transmitter, and its antenna adopts a vertically pointing method. During its operation, it has been found that cloud observation within the 2–3 km height range is often obscured by the presence of clear-air echoes, especially during the warm months of Beijing. Thus, the accurate detection of clear-air echoes in MMCR returns is very important for observing and researching boundary-layer cloud and precipitation.

Many papers have reported research on clear-air echoes. For example, Russell and Wilson (1997) studied the mechanism of clear-air echoes in the boundary layer and considered that there are two main scattering mechanisms for clear-air echoes. One is particle scattering, which is a point or thin-line echo, mainly caused by pollen, insects, birds, etc. The other is Bragg scattering, which is a layered echo, mainly caused by turbulent clumps in the atmosphere or uneven atmospheric refractive index.

For researching clear-air echoes caused by the scattering of insects and other particles, many studies have used centimeter-band and dual-polarization radars. For example, Kessinger et al. (2003) successfully identified clear-air echoes through analysis of Doppler weather radar echo characteristics, including local mean intensity, local standard variance, texture features, and vertical difference of reflectivity factor, from the three types of base data (reflectivity factor, radial velocity, and spectral width). Melnikov et al. (2015) used S-band dual-polarization radars to identify the asymmetry of biological scatterers through dual-polarization parameters. Gauthreaux and Diehl (2020) and Yin et al. (2018) also analyzed the clear-air echoes caused by biological scatterers by using dual-polarization characteristics. Though polarization measurement is an efficient way to discriminate clear-air echoes from cloud echoes, polarization measurements are not equipped in standard radars of operational radar networks.

Relatively, there are few studies on clear-air echoes in the millimeter-wave band and layered echoes. Luke et al. (2008) extracted some features of clear-air echoes, including the derivative spectrum, main spectrum peak width, and the average Doppler velocity. By utilizing a back-propagating (BP) neural network for feature training and classification, 92% of the clear-air echoes were successfully identified. However, clear-air echoes can also be the result of other reasons such as uneven atmospheric refractive index and turbulence. In addition, a large number of extracted fea-

tures may lead to low computation and recognition accuracy. Therefore, the method needs to be further improved with redundancy processing on the extracted features. Kalapureddy et al. (2018) proposed a method to filter the echoes caused by biota in MMCR, under the assumption that the cloud echo is more coherent, and uniform, and has a longer correlation period than the biological echoes. The method is simply based on the continuous vertical reflectivity factor profile for separating the cloud and non-hydrometeor returns. It uses a 4-s moving mean and standard deviation values of the reflectivity factor profile for statistical inspection to screen out the biota. This method can deal with isolated insects, but it also relies on polarization measurements to assist with the identification of high-density biota in the cloud.

This study is designed to take full advantage of the data from four instruments in clear-air echo identification: an MMCR, a laser ceilometer, an L-band radiosonde, and an all-sky camera. The laser ceilometer can provide the cloud base information, while the L-band radiosonde and the all-sky camera can provide the humidity profiles and sky images respectively. Together with the MMCR, the three instruments can improve the recognition rate of clouds and enhance the verification of clear-air echoes. In addition, a new algorithm that achieves feature extraction, feature selection, and identification of clear-air echoes based on a neural network (Bao et al., 2004) is proposed in this study, which is flexible enough to be employed in standard profiling radars without constraint to polarization measurements.

2.   Clear-air echo signatures

According to Clothiaux et al. (2000) and Geerts and Maio (2004), small insects produce strong radar echoes within the 2–3 km height range, especially over land and during warm seasons. The reflectivity factor of the radar echoes of these insects is comparable to that of clouds and precipitation, making the true cloud echoes easily contaminated by the clear-air echoes. Consequently, the cloud base is difficult to detect without using laser equipment.

In the study of Luke et al. (2008), the radar reflectivity factor range of insect echoes was found to be −35 to 0 dBZ on the 35-GHz MMCR reflectivity factor measurements. For layered clear-air echoes, they mainly appear in the atmospheric boundary layer, and often have strong inversions at low altitudes at night. Such echoes often occur near an inversion layer, a warming layer, and a layer with abrupt changes in refractive index. Tang (2014) observed that the height of such clear-air echoes is mainly between the ground and 4 km height. Kalapureddy et al. (2018) observed with a 35-GHz radar that the biota echoes were mostly below 1.7 km and fell within the reflectivity factor range of −50 to −20 dBZ.

In view of the above reviews, this paper focuses on using millimeter-wave single-polarization radar to observe the reflectivity factor measurements from 1 September 2015 to 31 August 2016, and analyze the distribution characteristics of clear-air echoes, which are below 3 km height and

have a reflectivity factor ranging from −36 to −4 dBZ. The reflectivity factor and velocity spectra data of 9 and 25 April 2016 were selected for detailed analysis, as shown in Figs. 1 and 2. It can be observed in Fig. 1 that the reflectivity factor range of the clear-air echoes is −36 to −4 dBZ; in Fig. 2, the reflectivity factor range is −36 to −16 dBZ. Additionally, the velocity variation of clear-air echoes in the velocity spectrum is greater than that of cloud echoes.

3.   Instruments and data

In the radar reflectivity factor measurements, the echoes appearing below the cloud are considered clear-air echoes, so the determination of the cloud base height is particularly important. The intention in this paper is to combine the MMCR and laser ceilometer to determine the cloud base height, and then use the L-band radiosonde and the all-sky camera to assist in judging the cloud information to verify the reliability of the estimated cloud base height. In this experiment, the distance between any two of the four instruments is within 200 m and their deployment locations are shown in Fig. 3. The four instruments are introduced in the following subsections.

3.1.   MMCR

The MMCR used in this study is located in the southern suburb observatory in Beijing. It operates at 8.6 mm wavelength and 35 GHz frequency. Its antenna scans the

sky in the vertical direction and its maximum height of observation is 15 km. The vertical spatial resolution is 30 m and the temporal resolution is 60 s. The major technical and subsystem parameters are listed in Table 1. The MMCR uses three vertically pointing observation modes to detect simultaneously, and each observation mode corresponds to a different pulse width. Table 2 shows the specific parameters of the three observation modes. Figure 4 is a schematic diagram of the MMCR's system configuration (Nashashibi and Ulaby, 2001), in which both indoor and outdoor parts are included.

The base data and power-spectrum data from the MMCR are used in this study. The base data comprise the reflectivity factor, velocity, and spectral width. The power-spectrum data are obtained from Fast Fourier Transform of the time-domain signal, and reflect the echo power distribution of different Doppler velocity. Each radar range corresponds to a power spectrum, which is composed of 256 spectral points, and each spectral point corresponds to a Doppler velocity. The power-spectrum data are closely related to the microphysics and dynamics in the cloud, and are critical for extracting the features of radar echoes.
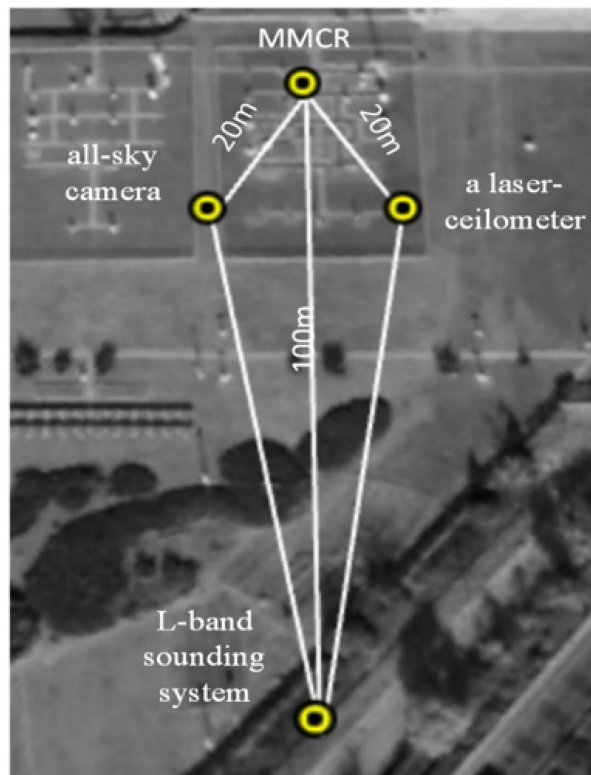
3.2.   Laser ceilometer

The laser ceilometer used in this study is Vaisala CL51, which is manufactured by Vaisala in Finland and certified by the CMA. Its maximum detection height is 15 km and its repeat frequency is 10 kHz, with a spatial resolution of
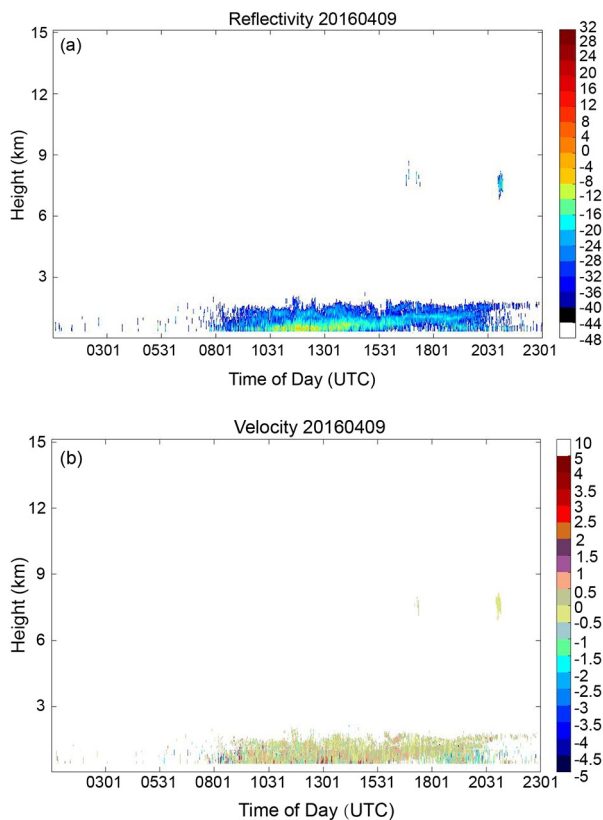
Fig. 1. (a) Reflectivity factor plot on 9 April 2016. (b) Velocity spectrum plot on 9 April 2016.
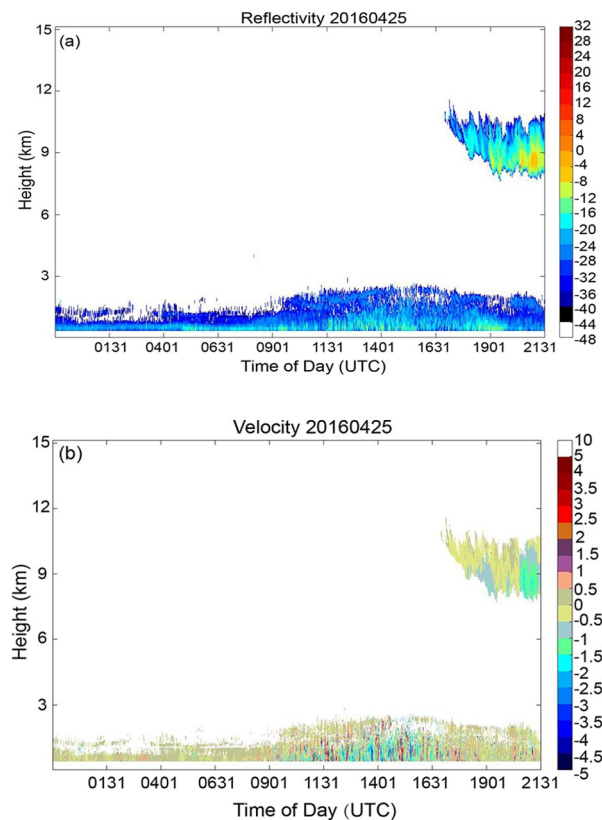
Fig. 2. (a) Reflectivity factor plot on 25 April 2016. (b) Velocity spectrum plot on 25 April 2016.

Fig. 3. Map of deployment locations of the MMCR, all-sky camera, L-band radiosonde, and laser ceilometer.

about 5 m and temporal resolution of 60 s.

The laser ceilometer emits continuous laser pulses vertically upwards. When the laser pulses enter and pass through the clouds from the cloud base, strong scattering at the cloud border will take place and the backscattered signal is received (He et al., 2011). Thus, the laser ceilometer can be used to assist in determining the cloud base height.

3.3. All-sky camera

The all-sky camera is designed to automatically monitor cloud conditions during daytime. Its camera above the instrument looks down at a hemispherical mirror with a heating device and takes the image of the sky reflected in the mirror. The average operation time of the camera used in this study is 0600–2000 Local standard time (LST hereafter). The all-sky images, with a resolution of 2848 × 4288 and 24

true colors, are taken every 10 min.

3.4. L-band radiosonde

In meteorological observation, the radiosonde system is important for upper-air observation. The maximum detectable height of the L-band radiosonde system is 30 km. The radiosonde sounding data used in this study are from the southern suburb observatory in Beijing, which are observed twice a day at 0715 and 1915 LST.

3.5. Detectability comparison between the MMCR and laser ceilometer

Discriminating clear-air echoes from cloud echoes becomes extremely challenging when the echoes mix in the lower level of the atmosphere, meaning it is necessary to first check the cloud detection ratios (the ratio between the time when one instrument detects the cloud and the time when both instruments are in operation) of the MMCR and the laser ceilometer for detecting clouds at different heights. The observed clouds are divided into three categories according to their base height. Clouds with a cloud base height of less than 2.5 km are low clouds, 2.5–4.5 km are middle clouds, and higher than 4.5 km are high clouds. Table 3 shows the cloud detection ratios of the MMCR and the laser ceilometer during selected observation times when both instruments were in operation.

It can be seen from Table 3 that the detection of high cloud, i.e., the cloud detection ratio of the MMCR, is larger than that of the laser ceilometer, which may be caused by the thin cloud particles of high clouds when backscatter to the laser ceilometer becomes weak and less detectable. For the detection of middle clouds, the MMCR and the laser ceilometer perform similarly, with only a slightly higher detection ratio for the MMCR. For low-cloud detection, the cloud detection ratio of the laser ceilometer is significantly higher than that of the cloud radar. Therefore, it is necessary to combine both instruments to determine the actual cloud base height accurately.

In accordance with commonly used indicators of statistical significance, we employ the t-test method for significance testing, with the level of significance (α) set to 0.05. The cloud base height detected by the MMCR and the laser ceilometer from 1 December 2015 to 31 January 2016 are

Table 1. Major technical parameters for the MMCR.

Item	Technical specifications
Radar system	Coherent, pulsed doppler, solid-statetransmitter, pulse compression
Radar frequency	35 GHz (Ka band)
Detecting parameters	Reflectivity factor (Z), vertical velocity (V), spectral width (W)
Transmitter peak power	$P_t \geqslant 50$ W
Antenna subsystem	Antenna type: Cassegrain
	Antenna diameter: 2.4 m
	Beam width: 0.25°
	Height: 0.120–15 km
Range of detection	Temporal resolution: 60 s (adjustable)
	Height resolution: 30 m

Table 2. Specific parameters of three observation modes for the MMCR.

Pulse width	2 μs	5 μs	20 μs
Minimum range	360 m	960 m	3060 m
Maximum range	2460 m	5010 m	18 510 m
Dwell time	4 s	4 s	4 s
Number of range bins	30–100	65–200	210–617
Range sample volume spacing	30 m	30 m	30 m

compared, as shown in the scatterplot in Fig. 5, and a clear linear correlation is shown, with a significant correlation coefficient of $R = 92\%$, which is greater than the t-test critical correlation coefficient and thus is significant. Therefore, the results show that the cloud base height observed by the MMCR and the laser ceilometer is consistent.

### 3.6. Comparison of the MMCR and L-band radiosonde

During 1–18 January 2016 and 1 April to 31 June 2016, a total of 109 days, there were 248 sounding observations from the L-band radiosonde. However, during the observation periods we selected, only 42 observations matched the MMCR observations. Similar as above, comparison of the performances of the MMCR and the L-band radiosonde on the detection of the cloud base indicated that they have consistent cloud base height observations, which is shown in Fig. 6. An example case analysis is presented below.

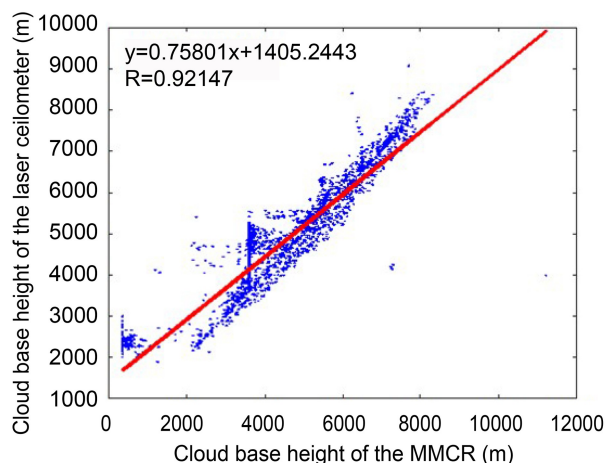Figure 7a shows the reflectivity factor profile of the

MMCR observed at 0701 LST 3 June 2016. Figure 7b shows vertical profiles of temperature and relative humidity observed by the corresponding radiosonde. As shown in Fig. 7a, the MMCR detected a cloud base at 6150 m, while the radiosonde detected a cloud base at 6517 m. They agree with each other reasonably well.
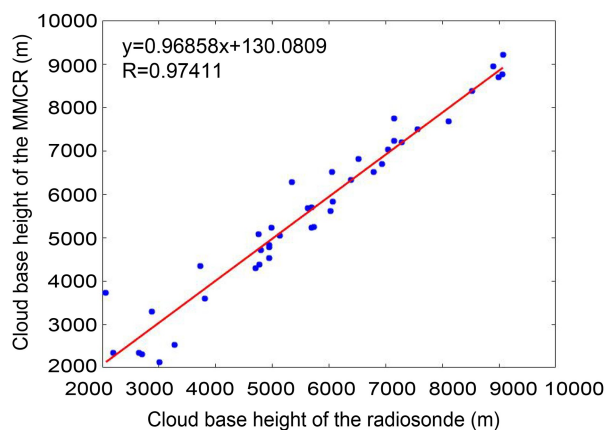
3.7. Benchmark for clear-air echoes

According to section 3.5 and the linear correlation shown in Fig. 5, the threshold of difference between the heights of the laser ceilometer and the MMCR is selected within 1000 m, which is also consistent with the results of Oh et al. (2016) and Zhao et al. (2017). With reference to the above consistent analysis among the instruments, as well as the study of Clothiaux et al. (2000), the benchmark samples for clear-air echoes can be derived: For a given MMCR observation, the cloud base height measured by the laser ceilometer at the same time is marked on the MMCR echoes. If the difference between the cloud base heights measured by the two instruments is within 1000 m, the cloud base height obtained by the MMCR is used as an actual cloud base height. Then, by analyzing the cloud information from the radiosonde data and examining the pictures from the all-sky camera, the reliability of the previously determined cloud base is further verified. If the result is reliable, the obtained cloud base height is used as the benchmark height. Echoes that appear above the benchmark
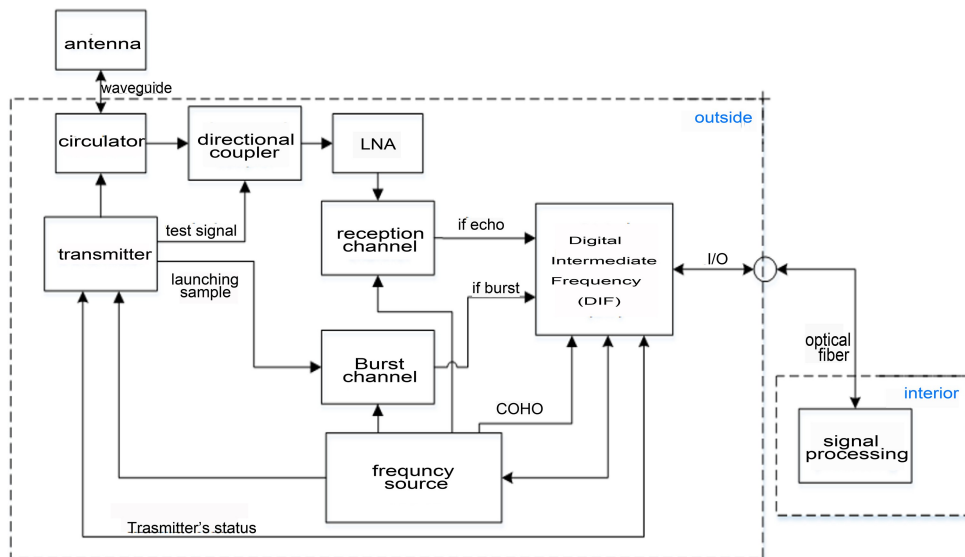
Fig. 4. Schematic diagram of the MMCR system configuration.

Table 3. Cloud detection ratio of the MMCR and the laser ceilometer in selected observation periods for clouds of different heights.

Cloud type	Selected observation time when both instruments are in operation (min)	Total time when MMCR detects cloud (min)	Total time when laser-ceilometer detects cloud (min)	Cloud detection ratio of MMCR (%)	Cloud detection ratio of laser-ceilometer (%)
Low cloud	420	265	402	63.1	95.7
Middle cloud	4394	3234	3086	73.6	70.2
High cloud	7808	6502	4115	83.3	52.7

Fig. 5. Cloud base height consistency of the MMCR and the laser ceilometer.

Fig. 6. Cloud base height consistency of the MMCR and the radiosonde.

height are considered as cloud echoes, and those appearing below the benchmark height are considered as clear-air echoes.

4. Description of the clear-air-echo recognition algorithm

4.1. *Procedures of the algorithm*

The flowchart in Fig. 8 shows the procedures of the clear-air-echo recognition algorithm. The procedures include feature extraction, feature selection, and clear-air-echo recognition.

Spectral features, including the power spectral kurtosis and spectral width, are effective in distinguishing cloud and clear-air echoes (Luke et al., 2008). The extraction of the spectral features is accomplished in three steps: (1) collection of clear-air and cloud echo samples; (2) extraction of spectral features of the samples; and (3) establishment of a set of features.

As introduced in section 3, the data from September 2015 to August 2016 are used in clear-air-echo recognition. After initial data screening, 54 834 radar echo samples can
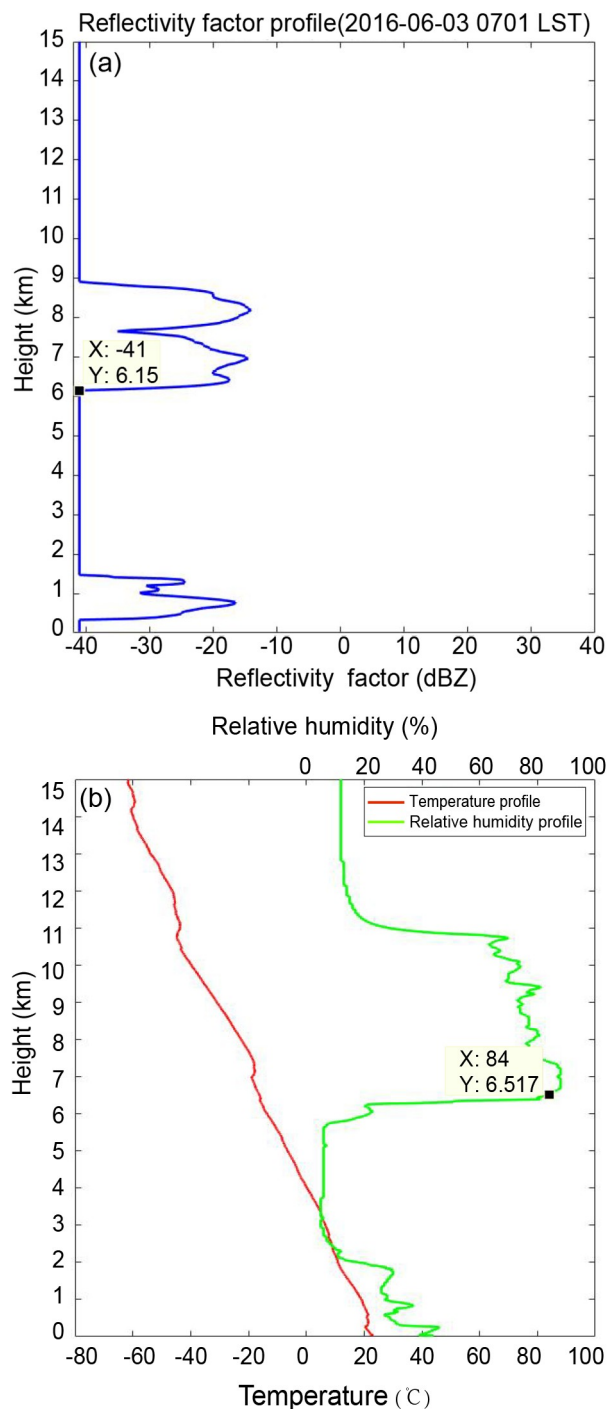
Fig. 7. (a) Reflectivity factor profile measured by cloud radar at 0701 LST 3 June 2016. (b) Temperature and relative humidity curves with altitude obtained from sounding at 0701 LST 3 June 2016.

be obtained to train the neural network. Among them, there are 11 706 clear-air echoes and 43 128 cloud-echo echoes.

From the analysis of the above established dataset, it is found that most of the clear-air echoes display a concentrated area of high-power spectral density along the velocity spectrum. They are multi-peaked with sharp fluctuations and narrow spectral width, compared to that of cloud echoes. Due to the existence of noises, the main spectrum,

which might contain meteorological signals, must be extracted first, and then the number of extreme points contained in this main spectrum is calculated. Assuming the radar noise is Gaussian white noise, the piecewise averaging method is used to remove the unwanted noises (Fabry et al., 1997). The specific steps of feature extraction are as follows:

(1) The entire spectrum is divided into 16 segments and the average value of each segment is calculated;

(2) The minimum mean value is used as the noise level;

(3) The signal-to-noise ratio of each spectral point is calculated;

(4) The threshold value of the signal-to-noise ratio is set, the points below this threshold are removed, and the main spectrum is retained.

Figures 9 and 10 show an example of the extracted main spectrum from clear-air echoes and cloud echoes. In order to better distinguish the clear-air echoes and cloud echoes, as many features as possible are extracted for the main spectrum. Presently, 28 features are extracted and are listed in Table 4 in section 4.2.

For all the extracted features, histograms are made and analyzed. For example, the reflectivity factor histogram is shown in Fig. 11, which shows that separating the cloud echoes from the clear-air echoes by the histogram of the reflectivity factor is possible. In most cases the reflectivity factor values of the two objects are obviously different, while in fewer cases the reflectivity factor values of the two objects are mixed, which makes it difficult to separate them with a high degree of accuracy. Therefore, by analyzing the degree of separation along the histograms of the features, the capability of each feature for distinguishing the two types of echoes can be evaluated.

4.2. *Feature selection*

In this study, there are 28 features (Table 4) extracted from clear-air echoes and cloud echoes. The purpose of constructing the sample feature set is to send the features of the clear-air echoes and cloud echoes to the neural network model for training, and let the algorithm model automatically learn the corresponding characteristics of the clear-air
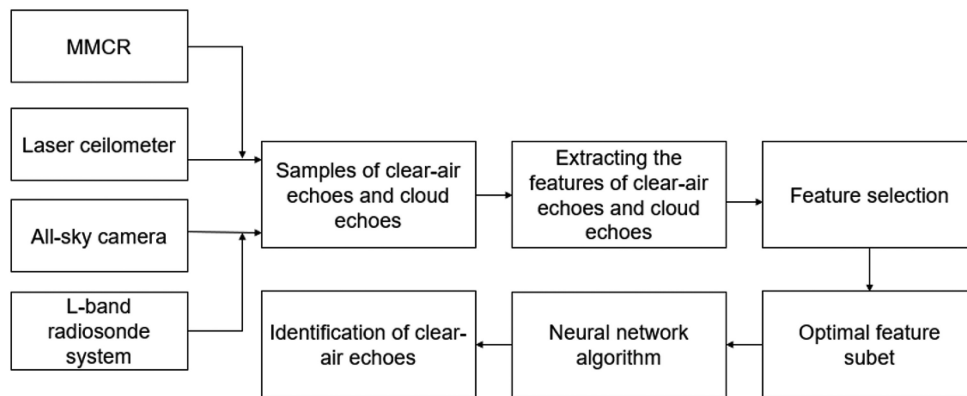

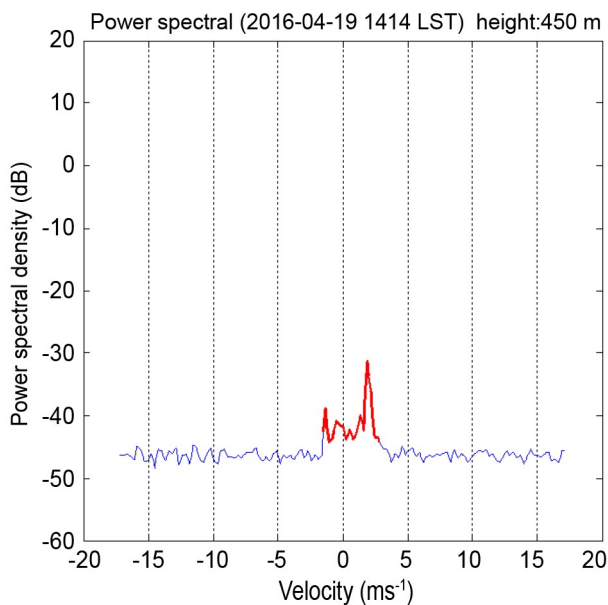Fig. 8. General framework of the algorithm for clear-air echo recognition.

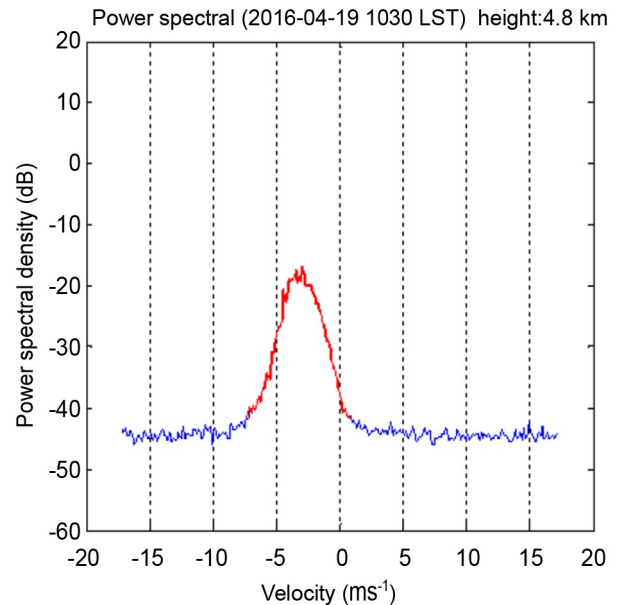Fig. 9. Extracted main spectrum (red) from clear-air echo at 450 m height at 1414 LST 19 April 2016.

Fig. 10. Extracted main spectrum (red) from cloud echo at 4.8 km height at 1030 LST 19 April 2016.

Table 4. The weight of each feature.

	Feature	Weight
1	Reflectivity factor Z	0.213
2	Doppler velocity V	0.028
3	Spectral width W	0.026
4	Spectrum width (SW)	0.049
5	Kurtosis (K)	0.048
6	Skewness (S)	0.035
7	Number of spectral peaks (NSP)	0.007
8	Location of spectral peak (LSP)	0.009
9	Mean of main spectrum (MMS)	0.123
10	Horizontal difference of reflectivity factor (Z_x)	0.018
11	Horizontal difference of doppler velocity (V_x)	0.004
12	Horizontal difference of spectral width (W_x)	0.003
13	Horizontal difference of spectrum width (SW$_x$)	0.001
14	Horizontal difference of kurtosis (K_x)	0.007
15	Horizontal difference of skewness (S_x)	0.023
16	Horizontal difference of number of spectral peaks (NSP$_x$)	0.026
17	Horizontal difference of location of spectral peak (LSP$_x$)	0.011
18	Horizontal difference of mean of main spectrum (MMS$_x$)	0.007
19	Vertical difference of reflectivity factor (Z_y)	0.010
20	Vertical difference of doppler velocity (V_y)	0.015
21	Vertical difference of spectral width (W_y)	0.001
22	Vertical difference of spectrum width (SW$_y$)	0.001
23	Vertical difference of kurtosis (K_y)	0.004
24	Vertical difference of skewness (S_y)	0.013
25	Vertical difference of number of spectral peaks (NSP$_y$)	0.019
26	Vertical difference of location of spectral peak (LSP$_y$)	0.007
27	Vertical difference of mean of main spectrum (MMS$_y$)	0.005
28	Height (H)	0.296
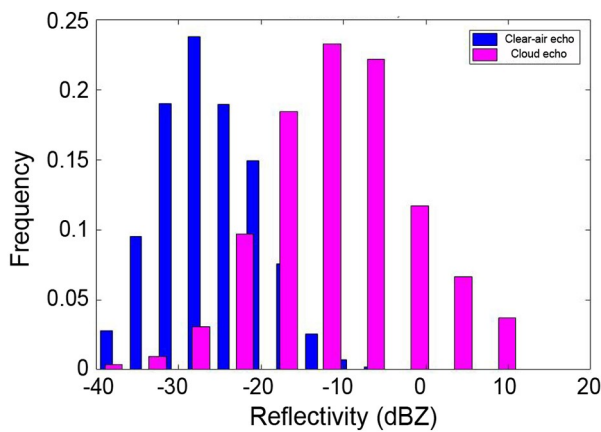
Fig. 11. Reflectivity factor including 11 706 clear-air echo sample points and 43 128 cloud echo sample points.

echoes and cloud echoes so that more accurate classification of clear-air echoes and cloud echoes can be achieved. The number of features is large and there is often redundancy between them, whose mutual information value is large. At the same time, the correlation between some features of the sample is not high. Therefore, if all the features are used for classification, the effect is not good and it also increases the complexity of subsequent learning algorithms.

Therefore, it is necessary to optimize the feature set and to form a feature subset. In this study, the Relief algorithm (Amjady et al., 2010) is used to achieve the feature selection.

The Relief algorithm is a nonlinear instance-based feature selection technique. In this study, the problem is to distinguish which class each sample belongs to—clear-air echoes or non-clear-air (or cloud in this case) echoes. Based on the correlation between the features and the classes, weights are calculated and assigned to the features of each sample. The weight reflects the ability of each feature to distinguish between the two classes.

Let $X = \{x_1, x_2, \cdots, x_n\}$ represent all n sample points including both clear-air and cloud echoes, and $x_i = [x_{i,1}, x_{i,2}, \cdots, x_{i,N}]^T$ represent the feature vector (a total of N features) of sample $x_i (i = 1, 2, ..., n)$. For a given randomly selected sample x_i, the algorithm will obtain the nearest sample to sample x_i as measured by the Euclidian distance in the feature space. The nearest sample of sample x_i in the clear-air echo class (near hit) is denoted as $H(x)$ and the one from the opposite class (near miss) is denoted as $M(x)$. The weight for the jth ($j = 1, 2, ..., N$) feature of sample x_i, $W_{i,j}$, is initialized as zero and updated during each iteration by the following:

$$W_{i,j} = W_{i,j} + |x_{i,j} - M_{i,j}(x)| - |x_{i,j} - H_{i,j}(x)|$$
$$(i = 1, 2, ..., n; j = 1, 2, ..., N) \,. \tag{1}$$

After a given number of iterations, the weight of all candidate features will be updated based on the selected samples. The weight of a feature represents its capability in classifying the samples based on that feature.

Using the above-mentioned Relief algorithm to perform a validity analysis on all the features in the sample feature set, the weight value of each feature can be obtained, which is shown in Table 4. In order to see the difference between each feature weight more visually, the results are shown in a bar chart in Fig. 12. Obviously, there are three features with larger weights than others, and their corresponding features are height ($H : 0.296$), mean of main spectrum (MMS : 0.123) and reflectivity factor ($Z : 0.213$), which form the optimal feature subset. This optimal subset of H, MMS, and Z will ultimately be used to achieve the classification of clear-air echoes and cloud echoes.

4.3. *Identification algorithm*

In this study, we use a feed-forward neural network architecture and the back propagation of error training algorithm (Bai et al., 2016). Figure 13 shows the framework of the neural network algorithm. The algorithm inputs the data from the input layer, processes it in the hidden layer, outputs the current result from the output layer, then enters the backward propagation, calculates the error between the predicted value and the true value, and sequentially derives the forward direction for each neuron. Then, the eigenvalues are updated to minimize the cost function by means of gradient descent, and the weights and thresholds of the connected neurons are updated according to the errors of the hidden layer neurons. This iterative process will be carried out in a cycle until the pre-set stopping conditions are reached. The details of the classification of cloud echoes and clear-air echoes using this algorithm are as follows.

The neural network includes one input layer, two hidden layers, and one output layer. The first hidden layer contains eight neuron units, the second hidden layer contains six neuron units, and the output layer has two neuron units. We take the three optimal features extracted earlier as inputs for the neural network, and the output is a vector of continuous values with a component for the possible classification. The output ranges from 0.0 to 1.0, representing in the meantime the confidence of a membership classification in each class, and will be treated as the input for the decision criterion. The decision criterion is a method of interpreting the neural network output vector and converting it into a discrete decision state. In this study, we use a "winner-takes-all" function to choose the output with the highest value as the classification result. The two neural network outputs are either clear-air echoes or cloud echoes.

5. Case study and results

This section presents the results by applying the above algorithm to the MMCR echoes. Due to instrument maintenance, the observation data of the four instruments are not continuous. At the same time, there are almost no clear-air echoes at the bottom of cloud radar echoes in winter in Beijing. Therefore, not every day's radar echoes can be used as a test sample to verify the effectiveness of the recognition algorithm. The MMCR's data from March 2016 to August 2016 are used, and there are 82 days of available data. The data samples can be divided into two different weather scenarios. The first is that the regions of cloud echoes and clear-air echoes are separate from each other. The second scenario is when regions of low cloud, clear-air echoes, and precipitation are all intermingled together at low levels of the atmosphere. The first-scenario radar echoes belong to simple weather conditions, and there are 54 days. The second-scenario radar echoes belong to complex conditions, and there are 28 days. In both scenarios, the number of cloud-echo and clear-air-echo points are counted before and after the algorithm recognition is performed, from which the clear-air-echo recognition rate is calculated.

Table 5 shows the statistics of the clear-air-echo recognition rate when the pixel points on the radar echoes are counted. For the simple radar-echo scenario, there are 513 409
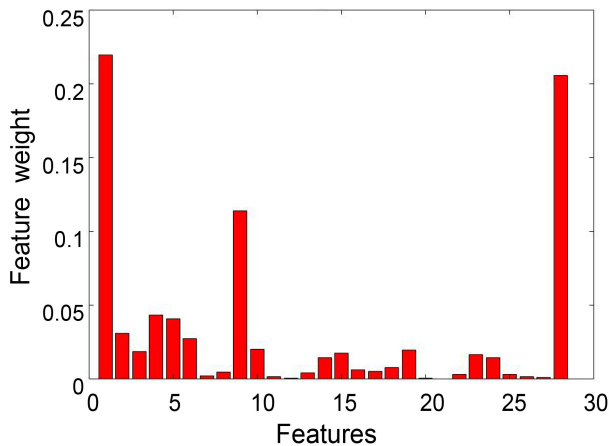

Fig. 12. Weight of each feature (feature 1: height; feature 9: spectral mean; feature 28: reflectivity factor).
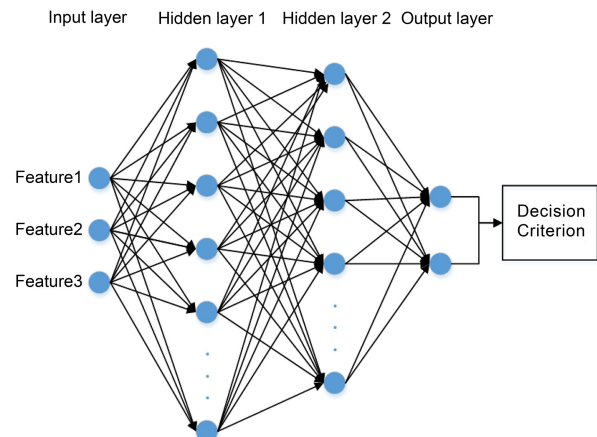

Fig. 13. Framework of the neural network algorithm.

Table 5. The clear-air-echo recognition rate.

Radar echo scenarios	Number of actual points before recognition		Number of points after recognition		Clear-air echo recognition rate
	Clear-air echo	Cloud echo	Clear-air echo	Cloud echo	
Simple	513 409	4 821 474	492 165	4 842 718	95.86%
Complex	420 896	3 321 780	371 998	3 370 678	88.38%

points being actual clear-air echoes and 4 821 474 points actual cloud echoes. After applying the recognition algorithm, the number of clear-air echoes being recognized is 492 165 and the number of cloud echoes is 4 842 718 with 21 244 clear-air echo points being recognized as cloud. Therefore, for these simple weather conditions, the clear-air-echo recognition rate is 95.86%. Similarly, in the complex weather scenarios, there are 420 896 points being actual clear-air echoes and 3 321 780 points actual cloud echoes. From the algorithm recognition, 371 998 points are recognized as clear-air echoes and 3 370 678 points as cloud echoes. Thus, the clear-air-echo recognition rate is 88.38% in the complex weather conditions.

For further evaluation of the new recognition algorithm, we used three cases that include simple and complex weather conditions. The data of 3 April 2016 were representative of a simple weather condition, while the data of 19 April and 27 April 2016 were representative of complex weather conditions. The three cases were excluded from the algorithm training, and are investigated in detail to test the validity and efficiency of recognition. The clear-air echoes and cloud echoes of the two days have already been verified with the data from the MMCR, the laser ceilometer, and the all-sky camera.

### 5.1. Simple weather condition: 3 April 2016

Figure 14a shows the observed reflectivity factor on 3 April 2016. The day was a cloudy day, and the regions of cloud and clear-air echoes were separate from each other. The echoes at heights above 3 km are cloud echoes while the echoes at altitudes below 3 km are clear-air echoes.

Because of the radar self-interference, the echo image displays some noises, such as the thin strips of echoes shown in Fig. 14a. Thus, a 3 × 3 convolution kernel of mean is used to smooth the radar echo images after filtering the clear-air echoes, and the outcome of the final filtered clear-air echoes is shown in Fig. 14b.

Overall, Fig. 14b illustrates a very satisfactory identification result, whereas the clear-air echoes are filtered out completely. By statistical analysis, there are 98 162 echoes in the original radar returns, and the number of clear-air echoes is 8931. The number of clear-air echoes in the original image that was correctly identified as clear-air echoes by the recognition algorithm is 8845, indicating that about 99.14% of clear-air echoes are successfully identified and eliminated.

5.2. Complex weather condition: 27 April 2016

Figure 15a shows the reflectivity factor of stratiform
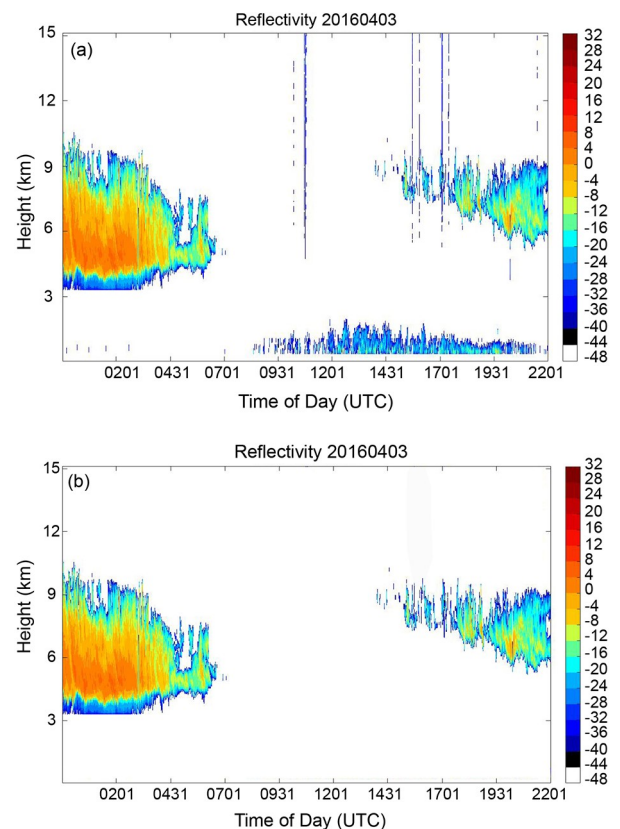
Fig. 14. (a) Reflectivity factor of 3 April 2016. (b) Result of reflectivity factor after filtering clear-air echoes.

clouds and clear-air echoes on 27 April 2016. We saved the reflectivity factor data samples of Fig. 15a and sent them to the trained BP neural network system. The BP neural network system recognizes the samples and divides all the samples into clear-air echoes and cloud echoes. Finally, we filtered out the clear-air echoes and showed only the samples of cloud echoes as shown in Fig. 15b. In this experiment, the new recognition method is very effective in terms of the overall recognition effect. The total number of samples of the echo points is 110 348 and the number of clear-air echo points is 22 376. Through the new algorithm in this paper, 91.25% of clear-air echoes are successfully identified. Comparing Figs. 14b and 15b, the size and thickness of clouds have no effect on the accuracy of the algorithm of identifying clear-air echoes.

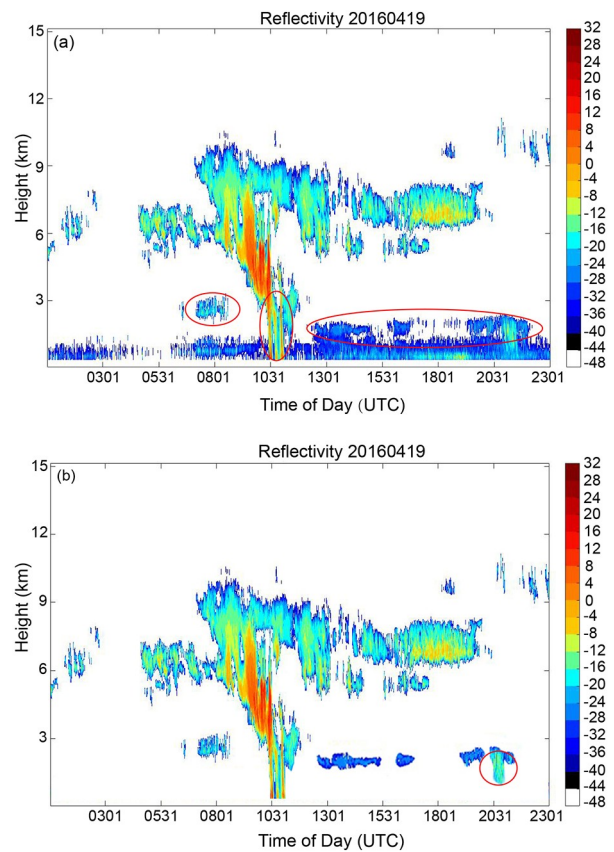### 5.3. Complex weather condition: 19 April 2016

Figure 16a shows a complicated distribution of reflectivity factor on 19 April 2016. In Fig. 16a, echoes of heights
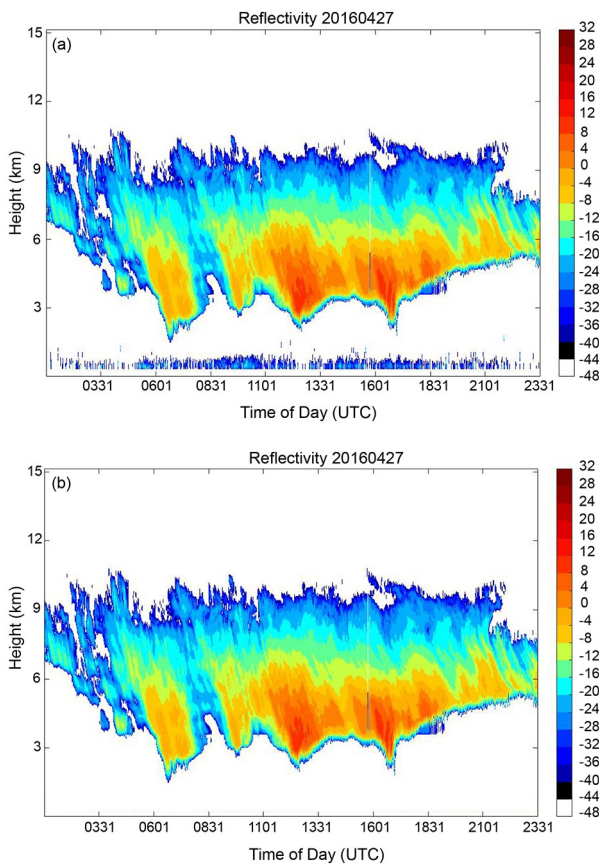
Fig. 15. (a) Reflectivity factor of 27 April 2016. (b) Result of reflectivity factor after filtering clear-air echoes.

Fig. 16. (a) Reflectivity factor of 19 April 2016, in which the circled echoes are confirmed clear-air echoes. (b) Result of reflectivity factor after filtering clear-air echoes.

above 3 km are cloud echoes while echoes of heights below 3 km are mixed with precipitation echoes, low cloud echoes, and clear-air echoes. It is known that the echoes from the elliptical circle in the area below the figure are cloud echoes or precipitation echoes by combining the laser ceilometer, the L-band radiosonde, and the all-sky camera. From the statistics, there are 118 635 echoes in the original radar images, and the number of clear-air echoes is 20 219. Like the processes of the filtering and recognition algorithm of clear echoes used for the previous case, the result after filtering out the clear-air echoes is shown in Fig. 16b. After recognition, there are 1887 clear-air echoes left, indicating a 90.67% recognition accuracy. Comparing Figs. 16a and b, we can see that some of the three echo regions of the marker are filtered out while the cloud echoes and precipitation echoes are retained. The part enclosed by the ellipse in Fig. 16b is a clear-air echo that is mistaken for cloud echo. The reason is that the reflectivity factor of the echo is too close to the reflectivity factor of the low cloud echo. Therefore, it is necessary to extract more features that can effectively distinguish cloud echoes from clear-air echoes.

Through the above case studies, our automatic recognition algorithm can effectively identify the clear-air echoes whether in simple cases or in the complicated situation of cloud-water mixing.

6. Conclusion

In this study, an algorithm is developed to automatically identify clear-air echoes in MMCR observations. The algorithm consists of three steps: feature extraction from the Doppler spectrum of the MMCR, optimization of the feature subset through feature selection using the Relief algorithm, and identification and filtering of clear-air echoes using the neural network algorithm. After all experimental data were counted, the recognition accuracy of clear-air echoes in simple and complex weather conditions reached 95.86% and 88.38%, respectively. Finally, we show three experimental cases and give the corresponding recognition effect of clear-air echoes. One of them is a relatively complicated case where the cloud and clear-air echoes are intermingled due to precipitation, while the other two are simple cases where the cloud and clear-air echoes are separate.

From the case studies, it is recognized that the method has a technical challenge and needs to be improved in future studies. The feature extraction method needs to be improved to extract the features that are more efficient in distinguishing clear-air echoes from clouds.

REFERENCES

Amjady, N., A. Daraeepour, and F. Keynia, 2010: Day-ahead electricity price forecasting by modified relief algorithm and hybrid neural network. *IET Generation, Transmission & Distribution*, **4**(3), 432–444, https://doi.org/10.1049/iet-gtd.2009.0297.

Bai, Y., Y. Li, X. X. Wang, J. J. Xie, and C. Li, 2016: Air pollutants concentrations forecasting using back propagation neural network based on wavelet decomposition with meteorological conditions. *Atmospheric Pollution Research*, **7**, 557–566, https://doi.org/10.1016/j.apr.2016.01.004.

Bao, Y. D., Y. P. Wu, and Y. He, 2004: Optimal Mix forecasting method based on BP neutral network and its application. *Journal of Agricultural Mechanization Research*, **3**, 162–164, https://doi.org/10.13427/j.cnki.njyi.2004.03.074.

Clothiaux, E. E., T. P. Ackerman, G. G. Mace, K. P. Moran, R. T. Marchand, M. A. Miller, and B. E. Martner, 2000: Objective determination of cloud heights and radar reflectivities using a combination of active remote sensors at the ARM CART sites. *J. Appl. Meteorol.*, **39**(5), 645–665, https://doi.org/10.1175/1520-0450(2000)039<0645:ODOCHA>2.0.CO;2.

Fabry, F., C. Frush, I. Zawadzki, and A. Kilambi, 1997: On the extraction of near-surface index of refraction using radar phase measurements from ground targets. *J. Atmos. Oceanic Technol.*, **4**, 978–987, https://doi.org/10.1175/1520-0426(1997)014<0978:OTEONS>2.0.CO;2.

Frisch, A. S., C. W. Fairall, and J. B. Snider, 1995: Measurement of stratus cloud and drizzle parameters in ASTEX with a Kα-band Doppler radar and a microwave radiometer. *J. Atmos. Sci.*, **52**, 2788–2799, https://doi.org/10.1175/1520-0469(1995)052<2788:MOSCAD>2.0.CO;2.

Gauthreaux, S., and R. Diehl, 2020: Discrimination of biological scatterers in polarimetric weather radar data: Opportunities and challenges. *Remote Sensing*, **12**(3), 545, https://doi.org/10.3390/rs12030545.

Geerts, B., and Q. Miao, 2004: The use of millimeter Doppler radar echoes to estimate vertical air velocities in the fair-weather convective boundary layer. *J. Atmos. Oceanic Technol.*, **22**(3), 225–246, https://doi.org/10.1175/JTECH1699.1.

He, J. F., W. Q. Liu, Y. J. Zhang, Z. Y. Chen, J. Ruan, and L. M. Wang, 2011: A denoising method for backscatter signal of laser ceilometer based on Hilbert-Huang transform. *Acta Optica Sinica*, **31**, 0201001, https://doi.org/10.3788/AOS201131.0201001. (in Chinese with English abstract)

Hogan, R. J., N. Gaussiat, and A. J. Illingworth, 2005: Stratocumulus liquid water content from dual-wavelength radar. *J. Atmos. Oceanic Technol.*, **22**, 1207–1218, https://doi.org/10.1175/JTECH1768.1.

Jacoby-Koaly, S., B. Campistron, S. Bernard, B. Bénech, F. Ardhuin-Girard, J. Dessens, E. Dupont, and B. Carissimo, 2002: Turbulent dissipation rate in the boundary layer via UHF wind profiler Doppler spectral width measurements. *Bound.-Layer Meteorol.*, **103**, 361–389, https://doi.org/10.1023/A:1014985111855.

Kalapureddy, M. C. R., and Coauthors, 2018: A simple biota removal algorithm for 35 GHz cloud radar measurements. *Atmospheric Measurement Techniques*, **11**, 1417–1436, https://doi.org/10.5194/amt-11-1417-2018.

Kessinger, C., S. Ellis, and J. Van Andel, 2003: The radar echo classifier: A fuzzy logic algorithm for the WSR-88D. Proc. 3rd Int. Conf. on Artificial Intelligence Applications to the Environmental Science, Benalmadena, Spain, AMS, 40–45.

Kollias, P., and B. Albrecht, 2000: The turbulence structure in a continental stratocumulus cloud from millimeter-wavelength radar observations. *J. Atmos. Sci.*, **57**, 2417–2434, https://doi.org/10.1175/1520-0469(2000)057<2417:TTSIAC>2.0.CO;2.

Kollias, P., B. A. Albrecht, R. Lhermitte, and A. Savtchenko, 2001: Radar observations of updrafts, downdrafts, and turbulence in fair-weather cumuli. *J. Atmos. Sci.*, **58**, 1750–1766, https://doi.org/10.1175/1520-0469(2001)058<1750:ROOUDA>2.0.CO;2.

Lu, Y. H., K. Aydin, E. E. Clothiaux, and J. Verlinde, 2015: Retrieving cloud ice water content using millimeter- and centimeter-wavelength radar polarimetric observables. *J. Appl. Meteorol. Climatol.*, **54**, 596–604, https://doi.org/10.1175/JAMC-D-14-0169.1.

Luke, E. P., P. Kollias, and K. L. Johnson, 2008: A technique for the automatic detection of insect clutter in cloud radar returns. *J. Atmos. Oceanic Technol*, **25**, 1498–1513, https://doi.org/10.1175/2007JTECHA953.1.

Melnikov, V. M., M. J. Istok, and J. K. Westbrook, 2015: Asymmetric radar echo patterns from insects. *J. Atmos. Oceanic Technol.*, **32**, 659–674, https://doi.org/10.1175/JTECH-D-13-00247.1.

Nashashibi, A., and F. T. Ulaby, 2001: Millimeter-wave radar detection of partially obscured targets. Proc. 2001 Antennas and Propagation Society Int. Symp. Held in Conjunction with: USNC/URSI National Radio Science Meeting, Boston, MA, USA, IEEE.

Oh, S.-B., Y.-H. Kim, K.-H. Kim, C.-H. Cho, and E. Lim, 2016: Verification and correction of cloud base and top height retrievals from Ka-band cloud radar in Boseong, Korea. *Adv. Atmos. Sci.*, **33**(1), 73–84, https://doi.org/10.1007/s00376-015-5058-y.

Paulsen, W. H., P. J. Petrocchi, and G. McLean, 1970: Operational utilization of the AN/TPQ-11 cloud detection radar. Air Force Cambridge Research Labs Instrumentation Papers, 166–168.

Russell, R. W., and J. W. Wilson, 1997: Radar-observed "fine Lines" in the optically clear boundary layer: Reflectivity contributions from aerial plankton and its predators. *Bound.-Layer Meteorol.*, **82**, 235–262, https://doi.org/10.1023/A:1000237431851.

Sassen, K., G. G. Mace, and Z. E. Wang, 1999: Continental stratus clouds: A case study using coordinated remote sensing and aircraft measurements. *J. Atmos. Sci.*, **56**, 2345–2358, https://doi.org/10.1175/1520-0469(1999)056<2345:CSCACS>2.0.CO;2.

Tang, Y., 2014: The scattering mechanism and analysis of clear-air echo. Nanjing: Nanjing University of Information Science and Technology. M.S. thesis, 67 pp, Nanjing University of Information Science and Technology. (in Chinese with English abstract).

Yin, J. P., C. Unal, and H. Russchenberg, 2018: Object-orient-

ated filter design in spectral domain for polarimetric weather radar. *IEEE Trans. Geosci. Remote Sens.*, **57**(5), 2725–2740, https://doi.org/10.1109/TGRS.2018.2876632.

Zhao, J., X. Z. Cao, T. G. Dai, Z. C. Wang, D. D. Chen, and D. Zheng, 2017: Comparative analysis of cloud observed by millimeter wave cloud radar and sounding. *Meteorological Monthly*, **43**(1), 101–107, https://doi.org/10.7519/j.issn.1000-0526.2017.01.011. (in Chinese with English abstract)